Defence Science Journal, Vol. 64, No. 6, November 2014, pp. 509-516, DOI : 10.14429/dsj.64.8111

Flow Around a Conical Nose with Rounded Tail Projectile for Subsonic, Transonic, and Supersonic Flow Regimes : A Numerical Study

Amitesh Kumar*, H.S. Panda, T.K. Biswal, and R. Appavuraj
*National Institute of Technology, Rourkela-769 008, India
Proof and Experimental Establishment, DRDO, Chandipur-756 025, India
*E-mail: kumar.amitesh.18@gmail.com

ABSTRACT

Flow around a conical nose with rounded tail projectile has been studied numerically for subsonic, transonic and supersonic flow regimes. The conic angle of the projectile is 10°. The inflow Mach numbers are 0.5, 0.9, and 1.5. Axisymmetric Euler's equations are solved for predicting the drag coefficient. It has been observed that even for a subsonic flow regime, the Mach number distribution is not uniform owing to the non-symmetric shape of the projectile. The predicted drag coefficients for subsonic, transonic, and supersonic cases are 0.018, 0.089, and 0.395, respectively. It was observed that rounded tail is a better option than boat tail so far drag force is concerned.

Keywords: Projectile, drag, supersonic flow, numerical modelling, nose angle

NOMENCLATURE

C_D	Drag coefficient
C_p	Specific heat capacity at constant pressure
h_t	Total specific enthalpy
Ma_{in}	Inflow Mach number
p	Static pressure
r	Radial distance
R	Characteristic gas constant
S	Surface area
T	Absolute temperature
$\mathbf{V}$	Velocity vector

Greek Symbols

α	Nose angle
β	Tail angle
ρ	Density

Subscript

∞	Free stream conditions

1. INTRODUCTION

Studying the aerodynamic characteristics of projectile is most important task in designing the projectile. The study reveals the individual role played by important parameters which must be considered while designing a projectile. One of the most important parameters is the prediction of drag which depends on the drag coefficient. The drag of the projectile decides the range and/or terminal velocity of the projectiles. Various options, in practice, for drag reduction are boat tailing, base cavity, and base bleed[1,2]. In this study instead of boat tail, a rounded tail has been considered. The drag is defined as the stream-wise component of the forces acting on the boundary surface[3]. The total drag of a projectile can be broadly divided into two categories: one arising due to viscous (skin friction) forces and the other resulting due to pressure forces[4]. The pressure drag is created by the normal forces to the boundary surface, while the viscous drag is created by the tangential forces[5]. Out of these two components, the drag resulting due to pressure force is dominant. Therefore, studying the distribution of pressure over the projectile's surface is important.

The projectile during its flight moves through subsonic, transonic, and supersonic flow regimes. The interaction of the projectile with the flow-field is complicated because of the presence of a shock wave. When a projectile is launched from a barrel, depending upon the Mach number of the exiting jet ahead of the projectile, a secondary blast wave may form behind the primary blast wave[6]. The flow-field becomes more complicated because of the interaction of the projectile, primary blast wave, and the secondary blast wave with each other. These interactions affect the aerodynamic characteristics drastically. The unsteady flow-field of a projectile launch has been studied by many investigators[7–11]. Chand and Panda[12] studied the projectile trajectory using simplified point mass approach which considered only the drag force and the gravity force. They have shown that even with the simplified approach, the predicted range, time of flight range, and the deviation were within 7 per cent of the experimental results which they acquired using Doppler radar. Dutta[13], *et al.* proposed two methods to extract the drag coefficient from the radar-tracked flight data of a cargo shell. The effect of perturbation on the trajectory and stability of motion of an FSAPDS projectile was studied by Acharya and Naik[14]. Watanabe[8], *et al.* studied the one-dimensional projectile overtaking problem. They concluded that the possible overtaking can be either subsonic or supersonic. Ahmadikia and Shirani[15] studied the transonic and supersonic over-taking of a projectile preceding a shock wave. They found that as the projectile passes through the

Received 22 August 2014, online published 13 November 2014

moving shock wave, it changes the flow-field features and pressure distribution dramatically. The drag force decreases and even becomes negative while the projectile takesover the shock wave. It should be noted that unsteady flow-field predictions depend on the initial conditions of the projectile and the flow-field. Usually, the steady-state solution for a given Mach number (at the free-stream conditions) is considered as the initial condition. Therefore, for studying the un-steady flow-field, it is extremely important to predict the initial condition more precisely, which ultimately affects the final predictions.

The present study aims to study the steady-state flow-field for a projectile moving in subsonic, transonic, and supersonic flow regimes. The emphasis is also placed on predicting the drag coefficient for the three flow regimes for a rounded tail projectile. For the same purpose, a two-dimensional axisymmetric model around the projectile has been solved for the Euler's equations along with the inviscid energy equation using finite volume method. The results obtained will provide a deeper insight into the fundamentals of aerodynamic characteristics of the projectiles.

2. MATHEMATICAL FORMULATION

The geometry of the projectile is shown in Fig. 1. The parameters kept constant are:

- the nose angle $\alpha = 10°$,
- the tail angle $\beta = 40°$,
- radius of the projectile $R = 60$ mm, and
- the length of the projectile $L = 1$ m.

These parameters are chosen to model the actual projectile with a little modification at the base which is assumed to have a rounded tail instead of the conventional boat tail; the effect of which is studied in more detail in this paper.

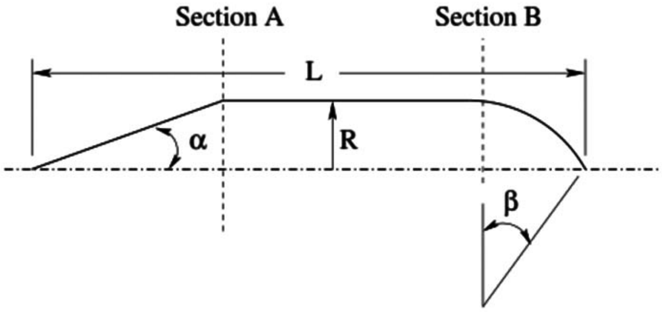

Figure 1. Geometry of the projectile.

2.1 Governing Equations

It should be noted that for the current study, the coordinates for the free Euler's equations are solved. The continuity and the momentum equations are written as:

$$\mathrm{div}\left(\rho\mathbf{V}\right) = 0 \tag{1}$$

$$\mathrm{div}(\rho u_i\mathbf{V}) = -\mathrm{div}(p\mathbf{i}_i) \tag{2}$$

where ρ is the density, $\boldsymbol{V}$ is the velocity vector, p is the static pressure. The momentum equation is written in index notation; $\mathbf{i}_i$ is the unit vector along the i th direction.

Along with the above mentioned continuity and momentum equations, the energy equation is also solved for the temperature distribution. In the absence of viscous effect, the energy equation simply reduces to the total enthalpy equation given by

$$h_t = C_p T + \frac{|V|^2}{2} \tag{3}$$

where h_t represents total enthalpy per unit mass, C_p is the specific heat capacity at constant pressure, and T is the absolute temperature. For the entire study, Eqn. (3) is solved for obtaining the distribution of temperature inside the computational domain. Once the distribution of pressure and temperature is obtained after solving Eqns (1) through (3), the density is updated using the equation of state:

$$p = \rho R T \tag{4}$$

where R is the characteristics gas constant.

2.2 Solution Approach

The two-dimensional axisymmetrical Euler equations are discretised on a structured non-orthogonal grid system using finite volume approach. A typical computational domain with variation in grid densities is shown in Fig. 2. Figure 2(b) shows the grid densities near the projectile. It should be noted that grids are laid in such a manner that grid density is higher near the large variation zone (i.e., near the projectile) and it is lower at the extremities of the computational domain. The upstream and the downstream distances of the computational domain are taken equal to 3 m and 15 m, respectively while the radial distance is taken equal to 8 m. The above-mentioned distances are found sufficient to impose the inflow and the outflow boundary conditions at the extremities of the domain. It should be noted that the continuity equation is used for solving pressure correction equation which takes into account the compressible nature of the flow. The discretisations of convective and diffusive terms (the term arising due to pressure correction equation)

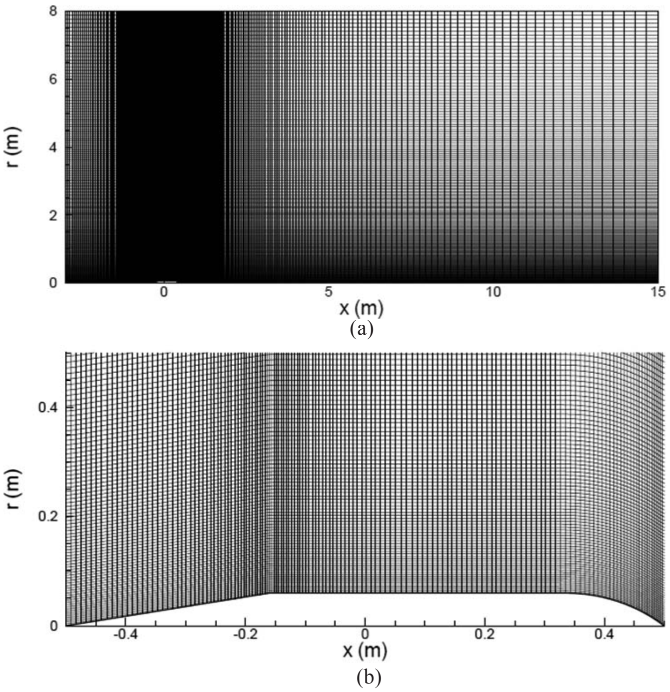

(a)

(b)

Figure 2. A typical computational domain and grid density near the projectile (a) A typical grid, and (b) Grid density near the projectile.

are done using deferred correction approach as suggested by Demirdzic[16], *et al*. The deferred correction approach not only enhances the accuracy of the numerical methods, as compared to the first-order schemes, but it also improves the stability of the numerical technique.

2.3 Discretisation Method

For numerical solution, the computational domain is divided into a number of smaller sub-domains, called as control volumes (CVs). A typical non-orthogonal control volume is shown in Fig. 3. The normal vector to each control volume face is represented by bold-italic letter *n*. All the primitive variables and all the fluid properties are stored at the control volume centres, represented by P, E, W, N, and S.

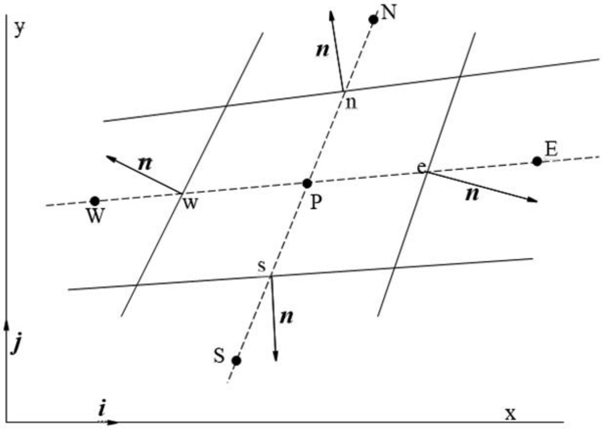

Figure 3. A typical non-orthogonal control volume with its neighboring elements.

It is to be noted that the current study uses coordinate free governing equations which do not depend on the curvature terms; it only requires the projections of the CV faces onto Cartesian coordinates during the course of discretisation. These are readily available with the current practice which joins the CV faces by straight lines. For example, mass flux at the east face is calculated as follows:

$$\dot{m}_e = \int_{A_e} \rho v \cdot n dS \approx (\rho v \cdot n)_e S_e \tag{5}$$

where unit normal vector at the east face is defined as

$$n_e S_e = (y_{ne} - y_{se}) r_e \mathrm{i} - (x_{ne} - x_{se}) r_e \mathrm{j} = S_x \mathrm{i} + S_y \mathrm{j} \tag{6}$$

Now, mass flux is given by:

$$\dot{m}_e = \rho_e (S_x u_x + S_y u_y)_e = \rho_e (v_n)_e \tag{7}$$

where v_n is the normal velocity component at the east face. Therefore, convective flux of any variable φ can now be expressed as

$$F_e^C = \int_{A_e} \rho \varphi v . n dS . \dot{m}_e \varphi_e \tag{8}$$

Similarly, the convective flux at the other CV faces can be found out.

After summing up contribution from all the convective fluxes and the source terms, the discretised equation for φ has the following form:

$$A_p \varphi_p + \sum A_{nb} \varphi_{nb} = Q_\varphi \tag{9}$$

where, A_{nb} accounts for the contribution from the neighbouring control volumes.

The Cartesian velocity components at each nodal location are obtained by solving the discretised Eqn (8) for u_x^* and u_y^*. These velocities, obtained using the old pressure and density, do not satify the continuity Eqn (1); that is why they carry an asterisk. The mass flux obtained using above velocities needs to be corrected to force the mass conservation; this is done by correcting the velocity and the density, which is described below.

Unlike the incompressible flow, the mass flux depends on both the velocity and the density in compressible flow. As noted earlier (Eqn (6), the mass flux at the CV faces is expressed in terms of the normal velocity component (v_n) and the density (ρ) at that location. To correct the mass flux, both these quantities are corrected and the corrected mass flux is given as

$$\dot{m}_e^{corr} = (\rho^* + \rho')_e (v_n^* + v_n')_e S_e \tag{10}$$

where ρ' and $v_{n'}$ represent the density and normal velocity corrections, respectively. The mass flux correction is thus given by:

$$\dot{m}_e' = (\rho^* v_n' S)_e + (\rho' v_n S) + (\rho' v_n' S)_e \tag{11}$$

The last term is usually neglected because it is of second order in corrections. The first term on the right hand side accounts for the velocity correction, the expression for which, in terms of pressure corrections, can be easily found out using the SIMPLE approach suggested by Patankar[17]. The second term arises due to the compressibility; it contains the density correction, which needs to be expressed in terms of pressure correction. This is achieved by[16]:

$$\rho' = \left(\frac{\partial \rho}{\partial p}\right) p' \tag{12}$$

The term $\left(\frac{\partial \rho}{\partial p}\right)$ can be determined from the equation of state or any other method which relates the pressure with the density. It should be noted here that the choice of $\left(\frac{\partial \rho}{\partial p}\right)$ does not affect the converged solution because all the corrections go to zero at the convergence. However, it does affect the convergence rate. For the present study, this term is calculated using the equation of state.

2.4 Grid-independent Test

The accuracy of the numerical method depends on the order of the discretisation scheme used for the different components appearing in the governing equations and the type and number of control volumes used for the simulation as well. Hence, it becomes extremely important to do grid-independence test before going for the productive runs. For example, Fig. 4 shows the variation of the pressure along the surface of the projectile for the two sets of grid density. It can be noticed that with the increase in number of control volumes, the change in predictions is almost negligible. Hence, a grid density of 420 × 240 is chosen for the entire simulations.

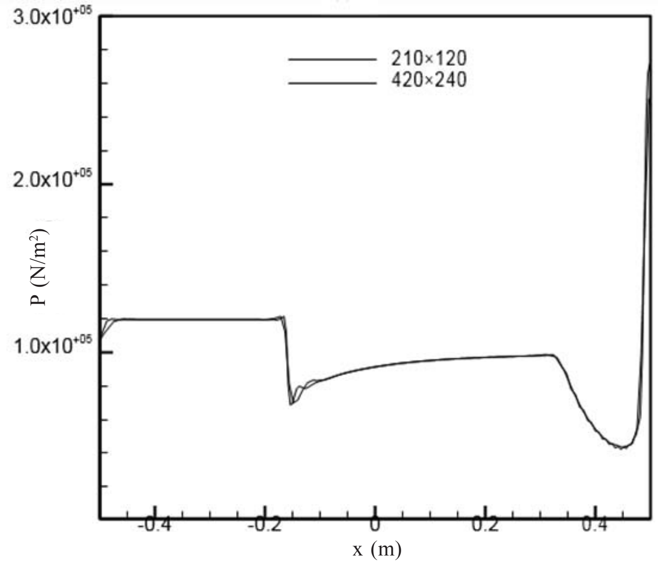

Figure 4. Grid-independency test.

2.5 Code Validation

The present numerical code is validated against the experimental results obtained by Mason[18], *et al.* for a plane, symmetrical, and converging/diverging nozzle of type A1. The geometrical details of the nozzle are given in literature[18]. The computational mesh consists of 450 × 50 control volumes for this case. It should be noted that higher grid density, e.g. 600 × 60, is also employed but the difference in results was insignificant. For the numerical computations, the total pressure and the total enthalpy are specified at the inlet while all the quantities are extrapolated from inside the computational domain at the outlet. Euler equations are solved by setting the viscosity value equal to zero. Figure 5 shows the variation of pressure and the isentropic Mach number on the channel wall. The figure also represents the experimental results obtained by Mason[18], *et al.* Their results are shown with a square symbol. It can be noticed that the current numerical prediction is matching quite well with the experimental result. Further note that, Fig. 6 indicates the capability of the employed numerical technique to resolve the shock wave clearly. Also, it can capture the reflection of the shock wave from the wall.

3. RESULTS AND DISCUSSION

The two-dimensional axisymmetrical Euler's equations along with the energy equation for inviscid fluid are solved. The input parameters, which are kept constant for whole of the simulations, are listed in Table 1. The drag coefficient and the flow pattern are obtained for all the compressible flow regimes: subsonic, transonic, and supersonic. For this purpose, the uniform inlet flow velocity is chosen in such a manner as to have an inflow Mach numbers of 0.5, 0.9, and 1.5 which correspond to the three flow regimes, respectively. In the following pressure variation plots, the surrounding atmospheric pressure is shown by a dashed line which is equal to 105 N/m².

3.1 Subsonic Flow Regime: Ma=0.5

Figure 7 represents the isomach lines and the Mach number and pressure distribution along the axis and the

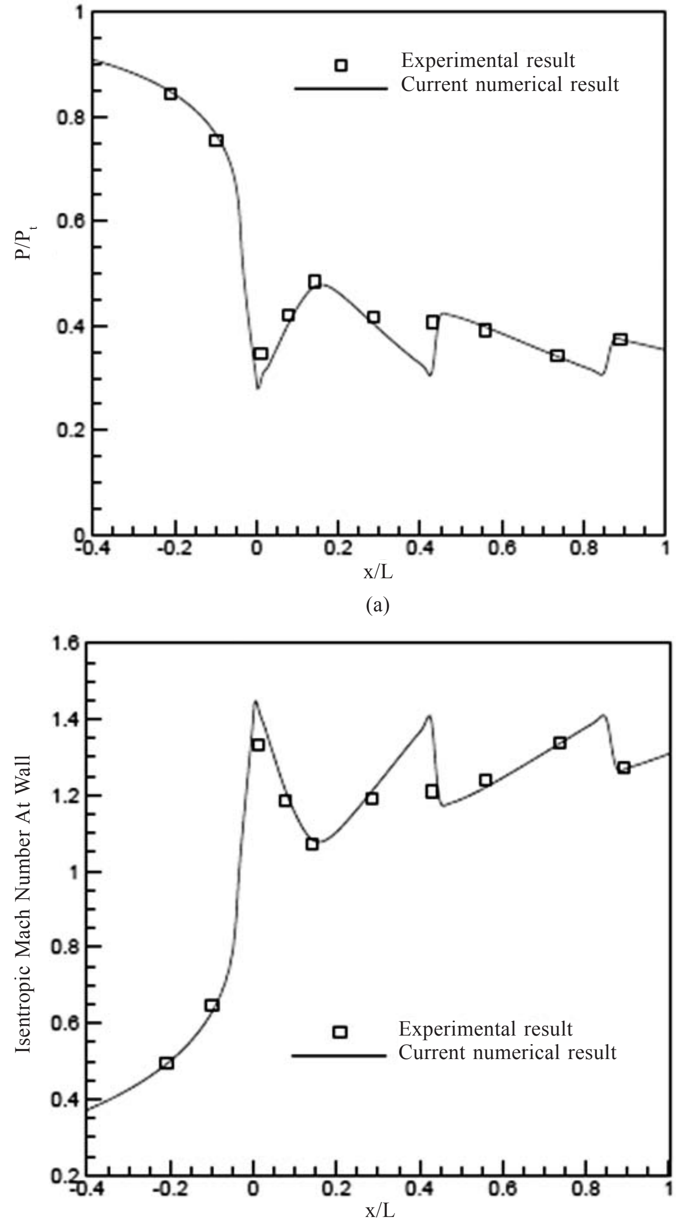

(a)

(b)

Figure 5. Pressure and isentropic Mach number variations along the channel wall : (a) Pressure variation, and (b) Isentropic Mach number variations.

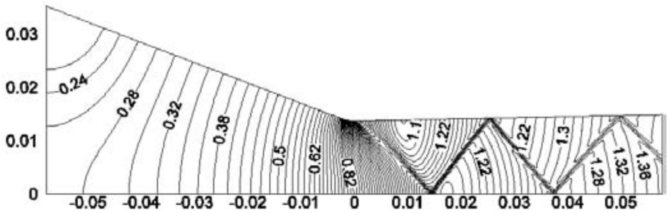

Figure 6. Mach number contours for the nozzle.

Table 1. Values of the input parameters

ρ_∞	1.2 kg/m³	γ	1.4; ratio of specific heats
C_p	1005 J/kg °C	R	287 J/kg °C
p_∞	105 N/m²	c_∞	340.17 m/s

projectile surface for a subsonic case. At the inlet, the upstream far field variables are specified (except for pressure). The inlet Mach number Ma_{in} is set equal to 0.5. It is noticed that even for a subsonic case the flow-field is not symmetric; the flow is decelerated near the trailing edge of the projectile because of the adverse pressure gradient there (as reflected in Fig. 7(c)). There are two locations on the projectile where the pressure gradient changes its sign. The two locations are identified as the merging point of the nose section to the main body (designated as section A in this study) and the merging point of tail section with the main body of the projectile (designated as section B in this study). It is noticed that there is a sudden drop in velocity at the nose tip (i.e., at $z = -0.5$), because of the stagnation of the flow-field at the nose tip. But, the flow accelerates afterwards till the section A, where it experiences a change in curvature of the projectile. This change slows down the flow till the start of section B where the flow again accelerates and then decelerates till the tail end. This is the point in the entire domain which experiences the maximum resistance; as a consequence, the Mach number is smallest at this point. The Mach number at the outlet is equal to the inflow Mach number, which is the characteristics of a subsonic flow[16,19,20].

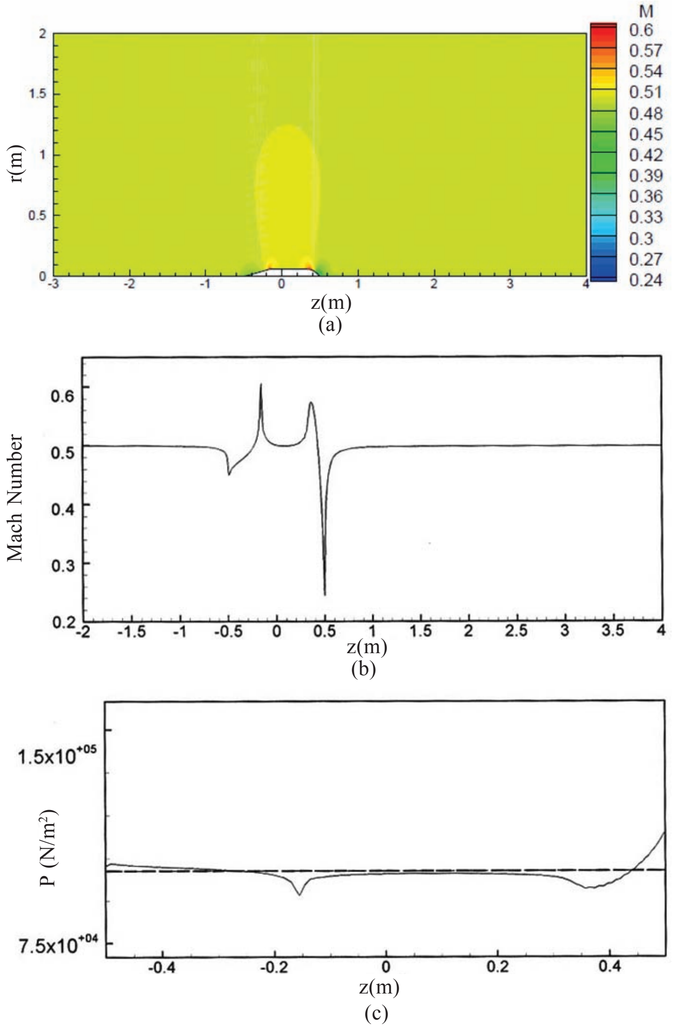

(a)

(b)

(c)

Figure 7. Mach number contours: (a) Mach number profiles, (b) pressure variation, (c) along the projectile, and the axis for subsonic inviscid flow.

3.2 Transonic Flow Regime: Ma = 0.9

When the inflow Mach number is increased to 0.9, the Mach number contours further deviate from being symmetric to the projectile. It is reflected in Fig. 8, which represents the isomach lines and the Mach number and pressure distribution along the axis and the projectile surface for a transonic flow regime. At the inlet, the upstream far field variables are specified (except for pressure). It can be noticed that the pressure variation remains almost similar with a change in the peak values. Also, it is observed that the first peak occurs exactly at the section A while the second peak shifts little downstream from section B. More or less pressure remains constant between sections A and B for both the cases. The maximum Mach number increased from 0.61 to 1.26, which occurs at the same location, z = -0.155 m, for both the cases.

3.3 Supersonic Flow Regime: Ma = 1.5

The effect of high speed on the drag is considered next. It is assumed that at the inflow boundary, i.e., the left boundary of the computational domain, the flow properties are uniform. The inflow velocity is chosen in such a way to make the inflow Mach number, $Ma_{in} = 1.5$. This condition corresponds to the

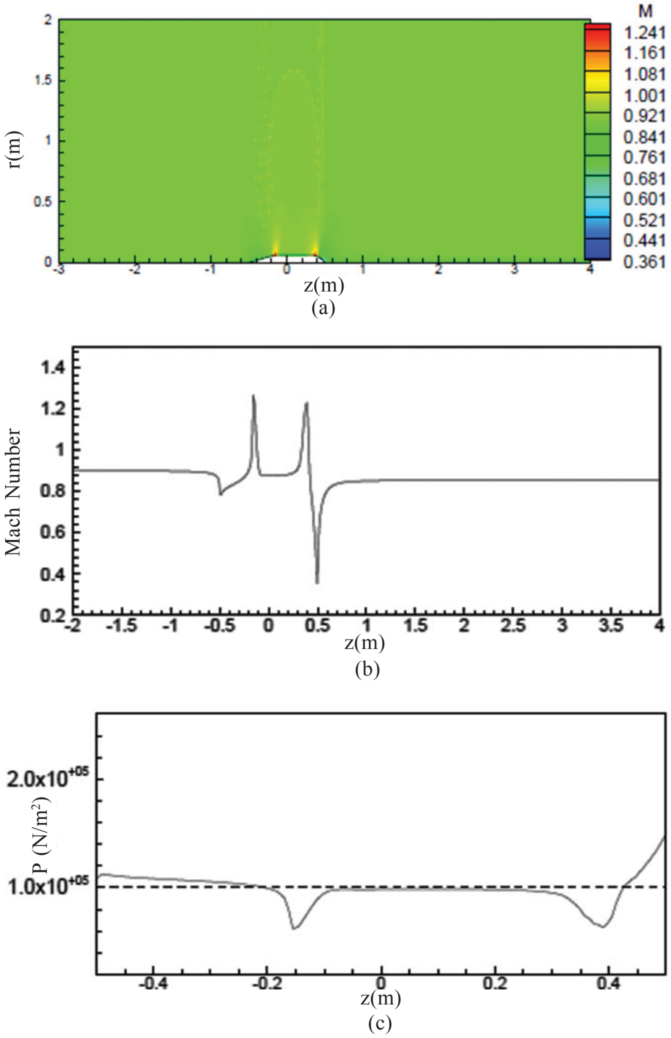

(a)

(b)

(c)

Figure 8. Mach number contours: (a) Mach number profiles, (b) pressure variation, (c) along the projectile, and the axis for transonic inviscid flow.

supersonic flow regime at the inlet. Also, the flow is supersonic at the outlet; therefore, all the variable values are extrapolated at the outlet. Figure 9 shows the isomach lines and the Mach number and pressure distribution along the axis and the projectile surface. This case shows entirely different patterns as compared to the previous two cases. Once the pressure increases at the nose tip, it continues to have almost the same value till the section A; as there is hardly any loss of kinetic energy between the nose tip and section A. At section A, there is a sudden change in flow properties, indicating the presence of shock wave at that location, which can be seen in Fig. 9(a). Another shock wave can also be noticed near the trailing edge of the projectile. It is interesting to observe that the flow decelerates between sections A and B, as opposed to previous two cases where the flow characteristics remained almost constant. Also, the pressure across the tail section remains sub-atmospheric and the fluid accelerates for long as compared to the previous cases. These features are in accordance with the features usually observed for high Mach number flows.

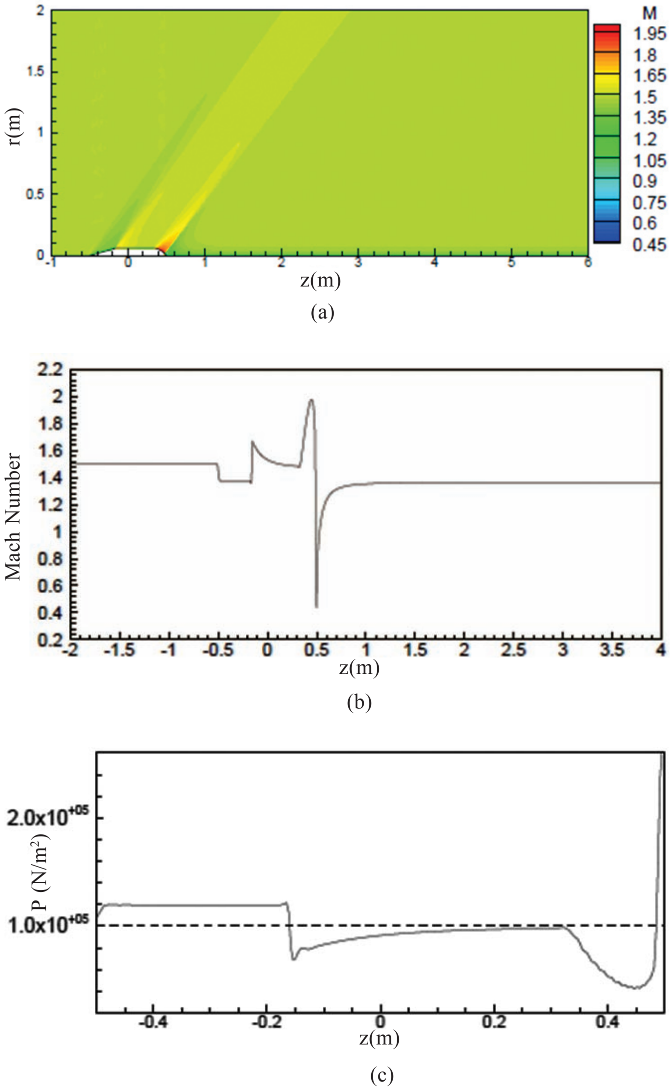

Figure 9. Mach number contours : (a) Mach number profiles, (b) pressure variation, (c) along the projectile and the axis.

3.4 Flow-field

Figure 10 shows the vector plot near the base of the projectile for the three cases. It can be noticed that the expansion waves are absent for the case of subsonic flow (Fig. 10 (a)). When the inflow Mach number is increased to 0.9, the intensity of flow increased around the base significantly; while this increase is only 10 per cent for subsonic case, it is around 33 per cent for the transonic case, i.e., Ma_{in} = 0.9. Although, the intensity of flow increased but there is no sign of any flow separation. This can be attributed to the two facts: (i) the curvature of base is smooth as opposed to the curvature of base for boat tail projectiles, and (ii) the assumption of flow tangency at the projectile surface. However, it should be mentioned that the viscosity does not have significant effect on the projectile aerodynamic characteristics[21]. Figure 10 (c) shows the vector plot for the supersonic case, i.e., Ma_{in} =1.5. The flow-field turns more towards the projectile surface owing to the presence of shock wave at the end of base.

3.5 Drag Coefficient

Drag plays an important role in the design of projectiles. Therefore, calculation was carried out to find out the coefficient of drag for the three flow regimes: subsonic, transonic, and supersonic.

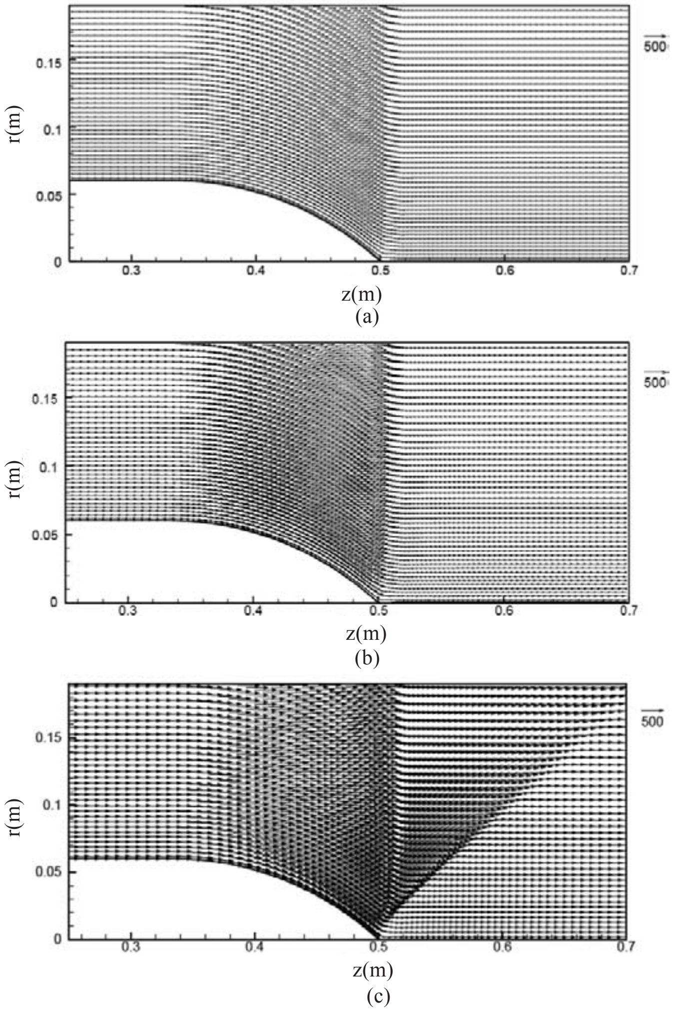

Figure 10. Vector plot near the base of the projectile : (a) Ma_{in}= 0.5, (b) Ma_{in}= 0.9, (c) Ma_{in}=1.5.

The coefficient of drag is calculated as

$$C_D = \frac{F_D}{\frac{1}{2}\rho_\infty A U_\infty^2}$$

where F_D is the drag force, ρ_∞ and U_∞ are the free stream density and velocity, respectively and A is the frontal area. The value of coefficient of drag for the studied cases is listed in Table 2. It can be noted from Table 2 that the drag coefficient for subsonic and transonic flow regimes decreases drastically as compared to the previous reported values for 155 mm artillery shell[15,22]. There is a decrease of about 90 per cent for subsonic case while it is nearly 75 per cent for the transonic case. This decrease is attributed to the smooth base profile of the projectile as the drag coefficient largely depends on the base profile. Also, it has been shown by Suliman[22], *et al.* that base drag reduces from 0.25 to 0.08 when the boat tail angle is increased from 0° to 14° for Mach number of 0.7. They observed a reduction of 50 per cent for both the subsonic and the transonic cases by increasing the boat tail angle by 9.50.

Table 2. Value of C_D for subsonic, transonic, and supersonic cases

Ma_{in}	0.5	0.9	1.5
C_D	0.018	0.089	0.395

4. CONCLUSION

An axisymmetric mathematical model has been developed for solving two-dimensional Euler's equations. Finite volume method is adopted for solution of the coordinate free governing equations. The drag coefficient is predicted using the developed model under subsonic, transonic, and supersonic flow regimes. It is shown that round-tailling of projectile reduces the drag by 90 per cent for the subsonic case, and by 75 per cent for the transonic case. It has also been observed that pressure variation along the surface of the projectile is similar for subsonic and transonic cases while the variation changes significantly for supersonic case, owing to the high-speed flow. As a result, the calculated drag coefficient for three cases comes out to be 0.018, 0.089, and 0.395.

REFERENCES

1. Carlucci, D.E. & Jacobson, S.S. Ballistics theory and design of gun ammunition. CRC Press, New York, 2008.
2. Moss, G.M.; Leeming, D.W. & Farrar, C.L., Military ballistics : A basic manual. Technical Report 1, Brassey's Ltd., UK.
3. Anderson, J.D. (Jr). Fundamentals of aerodynamics. McGraw-Hill Companies, New York, NY, 2010.
4. Sahu, J. Drag prediction for projectiles at transonic and supersonic speeds. Technical Report. US Army Ballistic Research Laboratory, Aberdeen Proving Ground, MD, 1986. Report No. TR-BRL-MR-3523.
5. Karman, T.V. Aerodynamics: Selected topics in the light of their historical development. Dover Publications Limited, Mineola, NY, 2004.
6. Sun, M. & Takakura, K. The formation of a secondary shock wave behind a shock wave diffracting at a convex corner. *Shock Waves,* 1997, **7**(5), 287–295. doi:10.1007/s001930050083
7. Jiang, Z.; Takayama, K. & Skews, B.W. Numerical study on blast flow-fields induced by supersonic projectiles discharged from shock tubes. *Phy. Fluids,* 1998, **10**, 277-288. doi:10.1063/1.869566
8. Watanbe, R.; Fujii, K. & Higashino, F, Numerical solutions of the flow around a projectile passing through a shock wave. *AIAA Journal*, 1995, **95**, 1790.
9. Takakura, Y.; Higashino, F. & Ogawa, S. Unsteady flow computations on a flying projectile within a ballistic range. *Computational Fluids,* 1998, **27**, 645–650. doi: 10.1016/S0045-7930(97)00055-8
10. Schmidt, E. & Shear, D. Optical measurements of muzzle blasts. *AIAA Journal*, 1975, **13**, 1086–1096. doi: 10.2514/3.60506
11. Merlen, A. & Dyment, A. Similarity and asymptotic analysis for gun firing aerodynamics. *J. Fluid Mech.,* 1991, **225**, 497–502. doi: 10.1017/S0022112091002148
12. Chand, K.K. & Panda, H.S. Mathematical Model to Simulate the Trajectory Elements of an Artillery Projectile Proof Shot. *Def. Sci. J.*, 2007, **57**(1), 139–148.
13. Dutta, G.G.; Singhal, A.; Kushari, A. & Ghosh, A.K. Estimation of drag coefficient from radar-tracked flight data of a cargo shell. *Def. Sci. J.*, 2008, **58**(3), 377–389.
14. Acharya, R.S. & Naik, S.D. Perturbation of initial stability of an FSAPDS projectile. *Def. Sci. J.*, 2006, **56**(5), 753-768.
15. Ahmadikia, H. & Shirani, E. Transonic and supersonic overtaking of a projectile preceding a shock wave. *Iranian Aerospace Society,* 2005, **2**(4), 45–53.
16. Demirdzic, I.; Lilek, Z. & Peric, M. A collocated finite volume method for predicting flows at all speeds. *Int. J. Numerical Methods Fluids,* 1993, **16**, 1029–1050. doi: 10.1002/fld.1650161202
17. Patankar, S.V. Numerical heat transfer and fluid flow. Hemisphere Publishing, Washington DC, 1980.
18. Mason, M.L.; Putnam, L.E. & Re, R.J. The effect of throat contouring on two-dimensional converging-diverging nozzle at static conditions. Technical Paper 1704, NASA, 1980.
19. Karki, K. & Patankar, S.V. Pressure based calculation procedure for viscous flows at all speeds in arbitrary configurations. *AIAA Journal*, 1989, **27**(9), 1167–1174. doi: 10.2514/3.10242
20. Ni, R. H. A multiple-grid scheme for solving the Euler equations. *AIAA Journal,* 1982, **20**(11), 1565–1571. doi: 10.2514/3.51220
21. Muthukumaran, C.K.; Rajesh, G. & Kim, H.D. The launch dynamics of supersonic projectiles. *J. Space. Roc.*, 2013, **50**(6), 1150-1161. doi: 10.2514/1.a32466
22. Suliman, M.A.; Mahmoud, O.K.; Sanabawy, M. A. & Hamid, O.E. Computational investigation of base drag reduction for a projectile at different flight regimes. *In* 13th International Conference on Aerospace Sciences & Aviation Technology, ASAT-13, 2009.

CONTRIBUTORS

Dr Amitesh Kumar is an Assistant Professor in the Deptt. of Mechanical Engineering at the National Institute of Technology Rourkela, India. He received his MTech and PhD in Mechanical Engineering from Indian Institute of Technology Kharagpur, West Bengal, India. His main research interests are computational fluid dynamics, computing high Mach number flows, turbulent flows, and laser materials processing. He has published more than 32 articles in the journals and conference proceedings.

Dr Himanshu Shekhar Panda received his MTech and PhD in Mechanical Engineering from IIT Kharagpur. Presently he is working as scientist-'E' at PXE, DRDO, India. His research areas includes : Experimental ballistics, computational fluid dynamics, spectral methods for scientific computing, microchannel flows in MEMS devices. Currently he is involved in high-speed flow visualisation and analysis and experimental impact dynamics studies. He is a Member of ADMB Panel under Armament Research Board.

Mr Tapan Kumar Biswal is currently working as a scientist at Proof & Experimental Establishment, Chandipur. He has 30 years of experience in the domain of high-speed imaging and photonics. His research interests include high-speed imaging and sensors.

Mr R. Appavuraj did his BE (Aeronautical Engineering) from Madras Institute of Technology, Chennai in 1982 and postgraduation from IIT-Madras, Chennai in 1984. Presently, he is Scientist-H and Director of Proof and Experimental Establishment (PXE), Chandipur. He has established the state-of-the-art Range Safety Simulation Model using soft computing techniques at ITR. He has published 30 conference papers and five research papers. He is recepient of *'DRDO Scientist of the Year Award'* in 2012 for his contribution towards development of real-time flight safety expert system.